


Article

# Hysteresis Passivation in Planar Perovskite Solar Cells Utilizing Facile Chemical Vapor Deposition Process and PCBM Interlayer

Chongqiu Yang , Xiaobiao Shan \* and Tao Xie \*

School of Mechatronics Engineering, Harbin Institute of Technology, Harbin 150001, China; yangchongqiu@hotmail.com

\* Correspondence: shanxiaobiao@hit.edu.cn (X.S.); xietao@hit.edu.cn (T.X.)

Received: 30 October 2019; Accepted: 25 November 2019; Published: 27 November 2019



**Abstract:** Low-cost, high-efficiency perovskite solar cells (PSCs) have the distinguished potential to be next commercialized photovoltaic devices. Chemical vapor deposition (CVD) process was regarded as an excellent choice as compared to solution deposition technique, however, the photovoltaic and stable performance of the former lags behind that of the latter. In this work, we propose a facile CVD pattern to fabricate PSCs, substrates covered by lead iodide ( $\text{PbI}_2$ ) sandwich-surrounded by the source methyl-ammonium iodide ( $\text{CH}_3\text{NH}_3\text{I}$ , MAI) powder. Heat and mass transfer, surface reactions are involved in the CVD deposition procedure. Numerical calculations present a uniform distribution of MAI vapor, contributing to homogeneous perovskite films with comparable surface morphologies, crystal structures and photovoltaic performances, despite of the notorious hysteresis. Herein, a PCBM ([6,6]-Phenyl  $\text{C}_{61}$  butyric acid methyl ester) interlayer is introduced before the  $\text{PbI}_2$  coating and the CVD process. Results show that even suffered from the torturous CVD procedure, the PCBM interlayer still works to passivating the bulk and interfacial recombination, reducing the hysteresis, improving the grain structure of perovskite films. Hence, the photovoltaic performance of PSCs enhances by 30%, and the filling factor difference between the forward and the reverse scan reduces to 6%.

**Keywords:** perovskite solar cells; chemical vapor deposition; uniform; recombination; hysteresis passivation

## 1. Introduction

Perovskite solar cells have attracted tremendous attention attribute to their remarkable properties, such as low-cost, easy-processing and tunable bandgap [1–3]. Planar perovskite solar cells (PSCs) are expected to prevail over mesoporous PSCs if the coating technique and interface engineering can be enhanced, due to the simplified fabrication process and economic benefits [4]. Based on the general spin-coating process, the promising chemical vapor deposition (CVD) process prefers to maintain a balance between the grain structure of lead iodide ( $\text{PbI}_2$ ) and the crystal growth of perovskite films [5–7].

Most research on CVD planar PSCs are dedicated to experimental fabrication, characterization and measurement, including various manufacturing processes with low temperature [8,9], low pressure [10,11], compositional engineering [12,13] and utilizing modified devices [14,15]. Recently, Lin et al. [16] investigated a stable 3D–2D planar heterojunction perovskite solar cell via fully vapor deposition by exposing in a methyl-ammonium iodide ( $\text{CH}_3\text{NH}_3\text{I}$ , MAI) vapor environment for 30 min under 180 °C. The non-encapsulation device shows a champion power conversion efficiency (PCE) of 16.50% and can maintain their efficiency under 55% relative humidity (RH) and 80 °C heating

stress. Qiu et al. [17] developed a fully vapor based scalable CVD process for depositing mixed cation perovskite films, achieving a PCE of approaching 10% on 10 cm × 10 cm substrates, demonstrating the potential of the CVD process for scalability. For numerical calculations and simulations, most current investigations are dedicated to the structural and material modification, overall performance of the entire PSC, without focusing on the delicate CVD or solution deposition process. Zandi and Razaghi [18] used the finite element simulation, trying to improve the efficiency of PSCs by numerically modification of the structural and material properties. However, more detailed numerical calculations on the manufacturing process seem to be outweighing the general efficiency-improving simulations. In order to completely figure out and promote the CVD process, it is essential to study the basic reaction kinetics with respect to operating conditions. In our previous work [19], FLUENT software (ANSYS Student 17.2, Canonsburg, PA., USA) was adapted to investigate the perovskite CVD procedure using a porous screen to obtain uniform mass flow distribution in the specified reaction zone at various temperature and pressure. Considering the sensitivity of perovskite precursor materials, it is tough to select and fabricate the desirable stuff in the actual experiments. Herein, this gives rise to figure out a simple improved CVD pattern to maintain uniform mass distribution and deposition reaction, regardless of the technically feasibility and material availability.

The morphology of perovskite films significantly influences the performance of PSCs [20–22]. As for the CVD-processed PSCs, the relationship between the perovskite grain structure and that of the  $\text{PbI}_2$  film is complicated due to the delicate synthesis reaction. Qiu et al. [23] demonstrated a three-step all vapor conversion route to fabricate methyl-ammonium lead iodide ( $\text{MAPbI}_3$ ) perovskite films with high crystallinity and purity. Bi et al. [24] investigated the PSCs using two-step spin coating process, indicating that a more hydrophobic bottom layer makes larger perovskite grain, which will form less grain boundaries and defects, better to the final PCE performance and stability [25]. According to previous report [26], PCBM ([6,6]-Phenyl  $\text{C}_{61}$  butyric acid methyl ester) is much more hydrophobic than the general titanium oxide ( $\text{TiO}_2$ ) as an alternative electron transport layer. Therefore, using PCBM bottom film as the electron transfer layer is supposed to generate larger perovskite grains than using  $\text{TiO}_2$ . Moreover, PCBM layer is also reported to passivate the surface and boundary defects to improve the hysteresis in solution-processed PSCs [27,28]. However, it is challenging to utilize the PCBM passivation layer in CVD-processed PSCs, due to the stability property of PCBM and the tough CVD thermal treatment.

In this work, we introduce a facile CVD pattern to produce  $\text{MAPbI}_3$  perovskite films, substrate covered by  $\text{PbI}_2$  sandwiched by the source MAI powder. Heat and mass transfer, surface reactions are involved in the CVD deposition procedure. FLUENT (ANSYS Student 2019 R3, Canonsburg, PA., USA) steady and transient calculations present an even distribution of MAI vapor and a uniform perovskite deposition reaction at the specified working conditions, producing homogeneous perovskite films despite of the notorious hysteresis of photovoltaic curves. In addition, a PCBM interlayer is introduced before the  $\text{PbI}_2$  coating and the CVD process. Results show that even suffered from the torturous CVD procedure, the PCBM still works to passivating the hysteresis, and improves the morphology of perovskite films to some extent. Moreover, owing to the excellent electron transfer ability of PCBM layer [26], the best PCE performance increases by 30%, and the filling factor (FF) difference between the reverse and the forward scan reduces to 6%.

## 2. Experimental and Simulation Methods

### 2.1. Sandwich CVD Pattern

Figure 1 presents the schematic diagram of CVD process for synthesizing perovskite  $\text{MAPbI}_3$  films. The quartz tube was purged by nitrogen ( $\text{N}_2$ ) prior to the power on, with vacuum evacuation to a desired pressure, about 30 mTorr in our case. The operating temperature was set to 120 °C, while maintaining the vacuum pump on during the whole deposition process. The quartz blocks were located at both ends in the quartz tube to obtain a homogeneous temperature distribution in the CVD

reaction zone. The  $\text{PbI}_2$  substrates were sandwich-surrounded by the  $(\text{CH}_3\text{NH}_3\text{I})$  MAI powder. As the MAI powder sublimates and diffuses in the quartz tube, the vapor MAI uniformly distributes around the  $\text{PbI}_2$  substrates to produce homogeneous perovskite films.

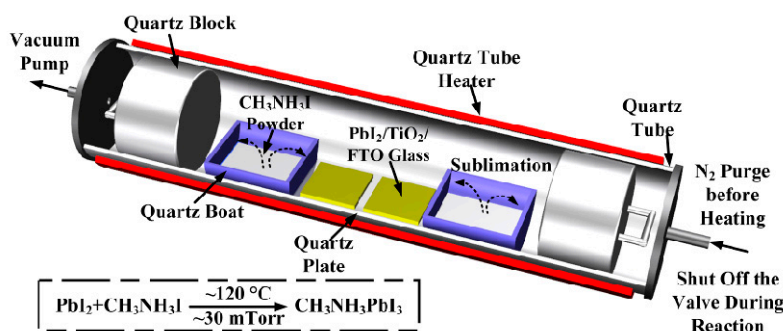


**Figure 1.** Schematic diagram of the chemical vapor deposition (CVD) process for synthesizing perovskite  $\text{MAPbI}_3$  films.

## 2.2. Device Fabrication and Characterization

The cells were fabricated using a similar method we reported previously [29] except the simplified sandwich CVD pattern as shown in Figure 1. The quartz tube is a commercialized chamber with dimensions of  $50 \text{ mm} \times 500 \text{ mm}$  (inner diameter  $\times$  length). The quartz boat was custom-made with dimensions of  $40 \text{ mm} \times 30 \text{ mm} \times 10 \text{ mm}$  (length  $\times$  width  $\times$  height). Planar n-i-p PSCs were fabricated with the architecture of  $\text{FTO}/\text{c-TiO}_2/\text{perovskite}/\text{Spiro-MeOTAD}/\text{Au}$ .

The FTO glass ( $25 \text{ mm} \times 25 \text{ mm}$ , Tec15, Pilkington) was laser-patterned and cleaned thoroughly. Next, 0.15 M titanium diisopropoxide bis (acetylacetonate) (Sigma-Aldrich, 75 wt.% in isopropanol, diluted with anhydrous ethanol) was used to deposit  $\text{TiO}_2$  compact film via the general spin coating process. For hysteresis passivation, a 10 mg/mL PCBM solution in chlorobenzene was spin-coated over the  $\text{TiO}_2$  layer. The vapor-assisted-solution process was adapted to fabricate perovskite films. A 1 M  $\text{PbI}_2$  was dissolved in anhydrous  $N,N$ -dimethylformamide (DMF) and dimethyl sulfoxide (DMSO) with the volume ratio of 9:1, then spun onto the  $\text{TiO}_2$  film with the air flow assisting process reported previously [29]. Using the sandwich CVD pattern as shown in Figure 1, the  $\text{PbI}_2$  substrates were located tightly in the middle of the two quartz boats without noteworthy gaps. The MAI powder was spread evenly inside the quartz boats. After vacuumed to about 30 mTorr, enable the CVD process at  $120 \text{ }^\circ\text{C}$  for 3 h. After cooling to room temperature, the Spiro-MeOTAD hole transporting layer was spun over the perovskite film [29], and the gold electrodes were masked using thermal evaporation. The active area for PCE characterization was  $9 \text{ mm}^2$ . All of the spin-coating and thermal annealing process were performed in ambient air.

A field emission scanning electron microscope (Zeiss Merlin, FE-SEM) was utilized to characterize the surface and cross-section morphologies of perovskite films, and the corresponding crystallinity was measured by X-ray diffraction (XRD, Siemens, Bruker-AXS D5005). Steady state photoluminescence (PL) spectra were recorded on a Hitachi F-7000 spectrometer with the wavelength scan range from 710 to 790 nm. The samples with configuration of  $\text{FTO}/\text{TiO}_2/\text{perovskite}$  and  $\text{FTO}/\text{TiO}_2/\text{PCBM}/\text{perovskite}$  without a hole transport layer were used to test the PL curves. Current density–voltage ( $J$ – $V$ ) measurements of the solar cells were performed by an Agilent B1500A semiconductor device parameter analyzer. A Newport ABB (94021A) solar simulator was employed to produce the AM 1.5G illumination ( $100 \text{ mW}/\text{cm}^2$ ) in ambient air. A Newport calibrated mono-Si reference cell was adapted to calibrate the light intensity of the solar simulator. The  $J$ – $V$  curves were obtained in the air with a voltage step size of 20 mV and a delay time of 50 ms, and the scan direction from forward to reverse (starting from 0 to 1 to 0 V) without any waiting time between the two bias scan measurements. The perovskite solar cells were pre-poled at open-circuit for long enough time to get an equilibrium state.

### 2.3. Simulation Methods

The calculations were carried out using a similar method we reported previously [19]. Figure 2 shows the 2D simulation diagram of MAPbI<sub>3</sub> deposition process in FLUENT with scale of about 1:2, simulating the fluid flow, mass and heat transfer during the surface deposition reaction. The model was initialized with a 100% isobaric N<sub>2</sub> fill. The outlet was set to be a pressure boundary condition of 30 mTorr. The operating and boundary temperature were all set to be 120 °C. The rest of the configurations for simulation referred to our previous work [19]. The two vapor MAI inlets were set to be a stable and constant mass flux. The mass diffusion of vapor MAI or N<sub>2</sub> in laminar flow were disciplined to Fick's law involving the Soret effect [30]. The thermal diffusion between the vapor MAI and the PbI<sub>2</sub> substrate for deposition reaction was defined using the kinetic theory. The deposition reaction rate of perovskite films was defined by the Arrhenius equation, with the pre-exponential factor of  $9 \times 10^{15}$  and activation energy of MAPbI<sub>3</sub> of 110 kJ·mol<sup>-1</sup> [31].

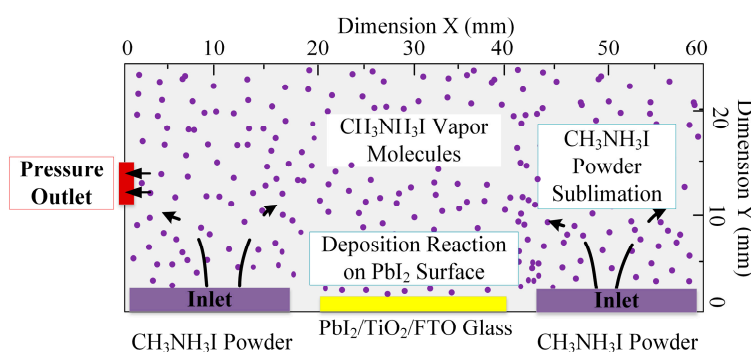
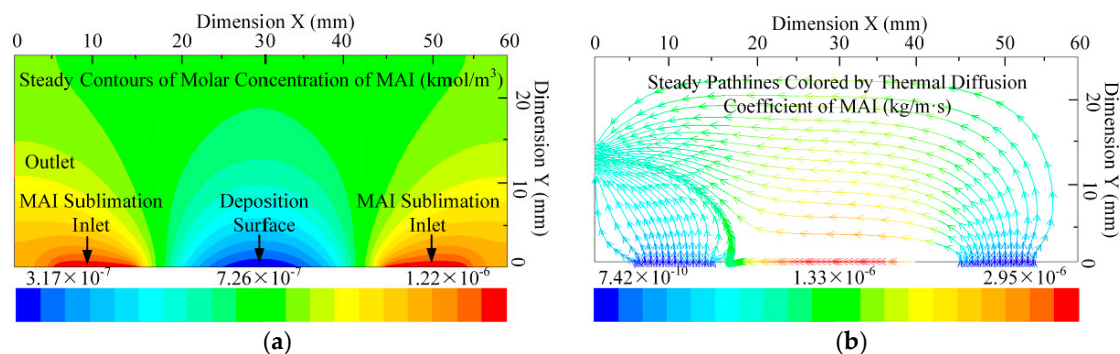


Figure 2. Simulation diagram of MAPbI<sub>3</sub> deposition process in FLUENT with scale of about 1:2.

## 3. Results and Discussion

### 3.1. Simulation Results and Discussion

A uniform vapor MAI mass distribution is crucial to deposit homogeneous perovskite films using the CVD method. Figure 3a presents the contours of molar concentration of MAI at the steady state. It looks like three distinct zones distinguished by the two sublimation inlets and the middle deposition surface. In spite of the asymmetrical arrangement of outlet, the distribution of vapor MAI seems to be symmetrical about the PbI<sub>2</sub> substrate. In the area directly above the deposition surface, the concentration of MAI is relatively lower than that of other areas with small gradient, owing to the consumption for perovskite synthesis reaction. The minimum concentration of MAI present above the PbI<sub>2</sub> substrate, where the most intense reaction occurs. Figure 3b shows the pathlines colored by the thermal diffusion coefficient of MAI. Well-distributed vapor MAI flows around the substrate surface, giving promise to a uniform perovskite film. The vapor deposition of perovskite films is controlled by the Arrhenius equation in this simulation, which gives dependence on absolute temperature. The apparent high value of thermal diffusion coefficient of MAI at the substrate surface also indicates its fierce synthesis reaction, same with Figure 3a. The diffusion length of MAI vapor molecules, as well as the reaction rate of perovskite deposition, are mainly dependent on the thermal diffusion coefficient [14]. In addition to the absorption and reaction occurred on the PbI<sub>2</sub> surface, the superfluous vapor MAI desorbed from the substrate surface and evacuated from the outlet.



**Figure 3.** Contours and pathlines of steady calculation results. (a) Steady contours of molar concentration of MAI and (b) steady pathlines from the inlets colored by thermal diffusion coefficient of MAI.

Based on the steady contours and pathlines of vapor MAI, a well-distributed MAI atmosphere around the reaction zone was achieved using the proposed sandwich CVD pattern, and the MAI can reach and adsorb onto the substrate surface to activate the perovskite synthesis reaction. Considering the homothermal condition inside the CVD tube compared to the general thermal treatment using a hotplate of the solution process, the  $\text{PbI}_2$  substrate located in the CVD tube here with uniform thermal boundary condition tends to produce a homogeneous perovskite film.

Figure 4 illustrates transient distribution curves of the molar concentration of MAI and the deposition rate of  $\text{MAPbI}_3$ . It is apparent that both the concentration of MAI and the deposition reaction of  $\text{MAPbI}_3$  tended to be uniformly distributed on the substrate surface with time going on. Although the curves of molar concentration of MAI still had a little bit curvature within the calculating time of 10 min, it was enough to satisfy a smooth and even perovskite film generation. Moreover, the deposition rate of  $\text{MAPbI}_3$  was proportional to the molar concentration of vapor MAI, indicating the mass-transport-limited growth at the initial stage. While the subsequent evolutions present a constant deposition reaction rate, indicating the thermodynamically limited growth at the steady stage. In comparison with Figure 3a, it is worth mentioning that the molar concentration of MAI had reached the steady (convergent) condition within 3 min, about  $0.3 \text{ mmol/m}^3$  at the center of the substrate surface. While the following successive CVD procedures smoothed the distribution of vapor MAI and maintained perovskite film deposition uniformly. Overall, the sandwich CVD pattern utilized here could realize a uniform distribution of vapor MAI and an even perovskite deposition reaction at the specified working conditions.

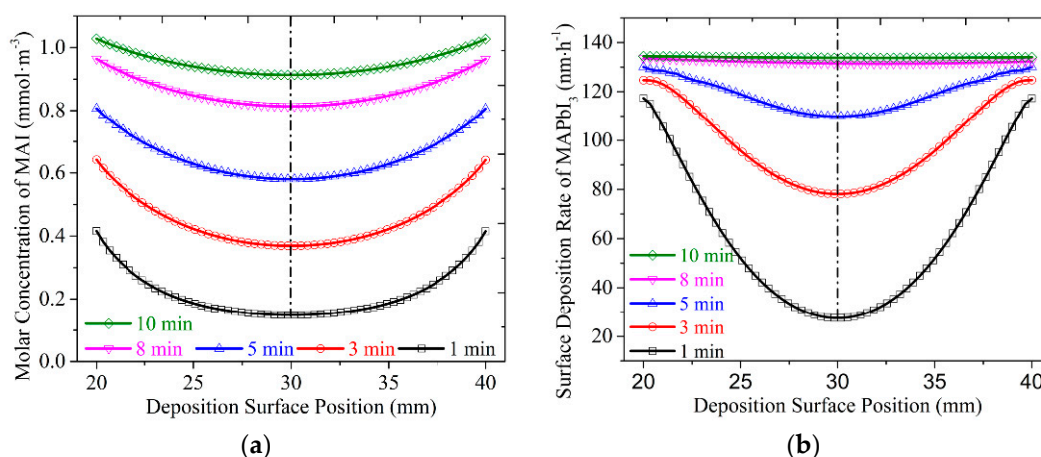


**Figure 4.** Transient distribution curves of the (a) molar concentration of MAI and (b) surface deposition rate of  $\text{MAPbI}_3$ . The dash dot lines specify the center of the  $\text{PbI}_2$  substrate surface.

### 3.2. Experimental Results and Discussion

As shown in the simulation section, uniform-distributed vapor MAI was supposed to obtain a homogeneous perovskite film using the proposed facile sandwich CVD pattern. In order to confirm the uniformity of the perovskite film, we investigated three different areas (left, middle and right) in one sample of the perovskite film, as seen in Figure 5a. Surface morphologies and the corresponding XRD curves in the specified areas are present in Figure 5. There were no obvious differences in grain size and crystallinity with fully coverage, except for plenty of small grain clusters in the left area. Figure 6 demonstrates the corresponding histograms of the perovskite grain size distribution shown in Figure 5 SEMs. More than 75% of the grains were between 200 and 400 nm in the three above-mentioned areas, with average grain sizes of 288 nm, 342 nm and 306 nm, respectively. However, perovskite grains appeared to be isolating with apparent grain boundaries and pinholes. The large and small perovskite grains were unfavorable to support an excellent photovoltaic performance of PSCs. Since large perovskite crystallites with a small level of grain boundaries and pinholes retard non-radiative charge carrier recombination, which enhance the open circuit voltage ( $V_{oc}$ ) of the cell [32]. The lack of the  $PbI_2$  diffraction peak indicates full conversion to perovskite crystals. The perovskite reflection peaks at  $2\theta = 14.15^\circ$  of the right and the middle areas were a little bit larger than that of the left area, indicating limited improvement of the crystallinity and larger grain size, in agreement with the SEMs and the histograms in Figure 6. Above all, it was reliable to obtain a uniform perovskite grain structure using the sandwich CVD pattern proposed in this work, although the crystallinity and compactness needed to be improved.

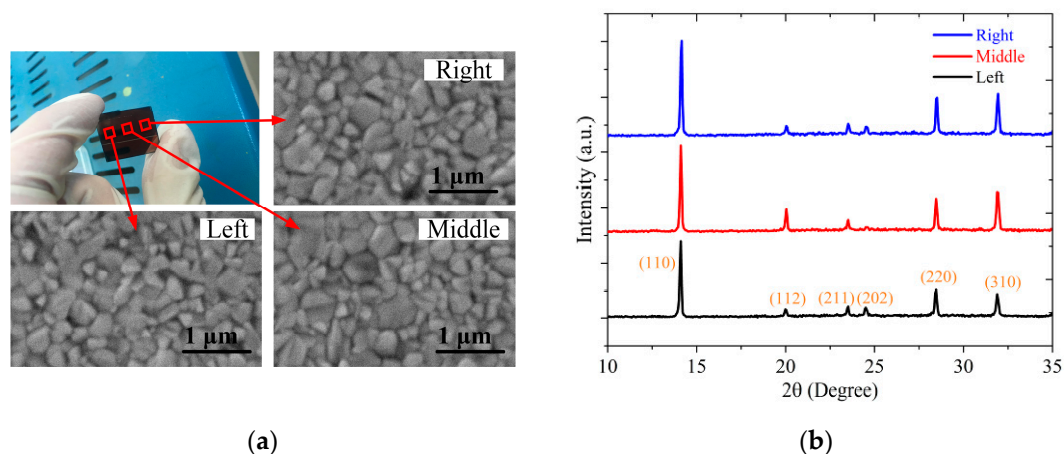


**Figure 5.** (a) Photograph and SEMs in specified area and (b) XRD curves corresponding to the specified area in (a).

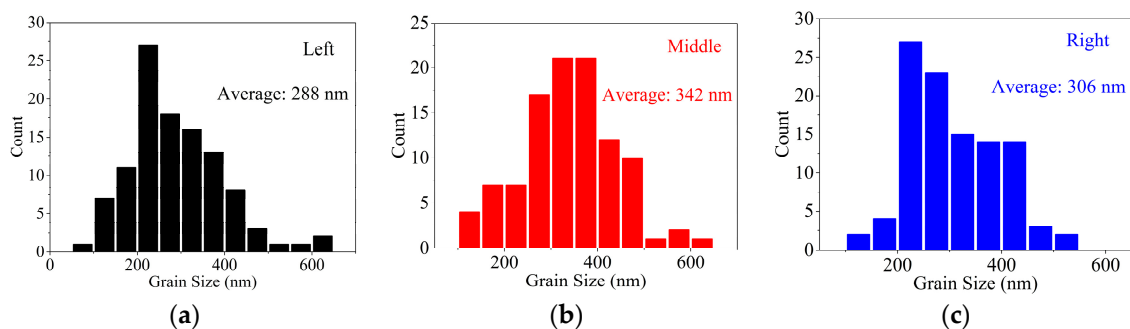


**Figure 6.** Histograms of the perovskite grain size distribution shown in Figure 5a SEMs: (a) left area; (b) middle area and (c) right area.

$J-V$  curve is the critical evaluation criterion for photovoltaic feature of a PSC. Figure 7 illustrates the  $J-V$  curves of the cell unit as specified in Figure 5a, and the corresponding photovoltaic arguments

were inserted. The perovskite solar cells fabricated in the proposed sandwich CVD pattern show similar  $J$ - $V$  curves, no matter whether it was the forward scan or reverse scan. At the beginning of the forward scan, the current density ( $J_{sc}$ ) dropped abruptly, leading to a poor filling factor (FF) and a severe hysteresis. As to the successive reverse scan, the shrunken current density maintained flat straight with a slight ‘bump’ (current maximum). Such hysteresis also generally occurred in many other researches, particularly the traditional defective planar PSCs [28]. The  $J$ - $V$  hysteresis could be interpreted by charge trapping and de-trapping process modulated by the irregular electric field. These observations implied the existence of abundant charge traps in the deposited perovskite films. The cell in the middle area with the highest PCE of 9.4% was obtained. In the case of  $V_{oc}$ , no large difference was observed between the two  $J$ - $V$  scans in all the three highlighted research areas, in agreement with the SEM and XRD tests, indicating similar grain boundaries, pinholes and homogeneous perovskite deposition process. The close-circuit current density presented an about 20%–30% difference between the two scan measurements. As for the FF of the reverse scan, it reached to about 60%–70% larger than that of the forward scan, indicating a massive hysteresis. Recently, Nemnes et al. [33] investigated the influences of measurement techniques on the dynamic  $J$ - $V$  performance, indicating that the extent and type of the  $J$ - $V$  hysteresis were dramatically dependent on the pre-poling conditions and the bias scan rate. The “S” shaped  $J$ - $V$  curves shown in Figure 7 were consistent with the findings in reference [33], if the perovskite solar cell was pre-poled at open-circuit, the forward scan curve present a crossover point with the following reverse scan curve.

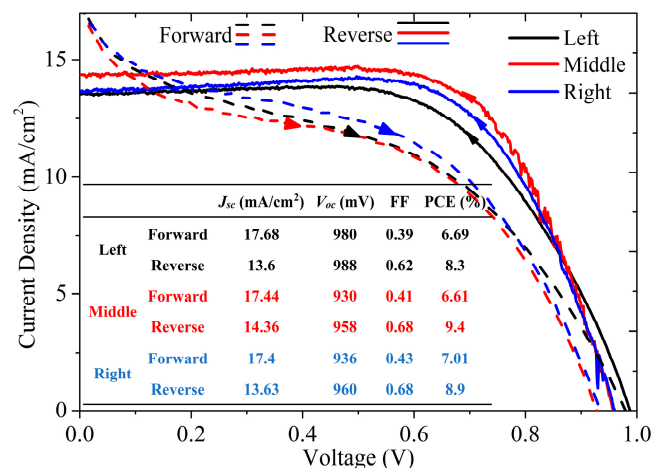


**Figure 7.**  $J$ - $V$  curves and corresponding photovoltaic performance of the perovskite solar cell (PSC) shown in Figure 5 with a scan step size of 20 mV and a standing time of 50 ms.

The overall PCE performances present here had no advantages compared to the excellent published work [34] due to the poor surface morphology and crystal quality of the perovskite films, on which our future work would focus. According to a recent numerical calculation [35] to investigate the  $J$ - $V$  hysteresis phenomenon, adapting the drift-diffusion model to simulate the ion vacancy moving inside the perovskite layer, the  $J$ - $V$  curves present in Figure 7 in well agreement with the dominant features of bulk recombination. As the scan conducts from the open-circuit to the close-circuit, the voltage reduction advanced the charge and ionic vacancy diffusion in the Debye layers, leading to a positive bulk electric field ( $E_{bulk}$ ), which eventually reached a maximum at the bump point. The maximum  $E_{bulk}$  was dedicated to split and transport the charge carriers to the corresponding contact layers, resulting in the current bump. Moreover, the noticeable reduction in current density at the beginning of the forward scan was also attributed to the steep decrease in  $E_{bulk}$ , which reduced the ability to separate the charge carriers to the corresponding transport layers and thereby increasing the bulk recombination inside of the perovskite layer. The shrunken current density of  $\sim 14$  mA/cm<sup>2</sup> in reverse scan compared to that of  $\sim 17.5$  mA/cm<sup>2</sup> in forward scan could be associated with the interfacial

recombination at the perovskite/TiO<sub>2</sub> interface, which caused by the trap states and defect pinholes. It is reported that the surface recombination could be passivated by appropriate interfacial interlayers for solution-processed PSCs [36,37], while it was unclear for CVD-processed PSCs, considering the degradation of the interlayer material during the rigorous CVD process.

From what was discussed above numerically and experimentally, we could state that the proposed facile sandwich CVD pattern using in this work was feasible to get a homogeneous perovskite film with comparable surface morphologies, crystal structures and photovoltaic performances, despite of the obvious hysteresis due to the defects induced bulk recombination and interfacial recombination.

Pronounced hysteresis is particularly observed in planar PSC using compact TiO<sub>2</sub> layer to extract electrons [27]. PCBM has been verified to serve to extinguish the hysteresis in inverted and regular device configurations fabricated by solution spin-coating [26,38]. It is unprecedented to introduce PCBM into CVD-processed PSCs. In this work, a PCBM interlayer was spun (2000 rpm, 4000 rpm and 6000 rpm for comparison) onto the top of the TiO<sub>2</sub> layer before the PbI<sub>2</sub> coating, followed by annealing at 100 °C in air for 5 min and CVD process at 120 °C. Figure 8 demonstrates the cross section, surface morphologies of the perovskite film with PCBM interlayer and the corresponding histogram of perovskite grain size distribution. Uniform perovskite crystal grains with fully coverage were observed. In addition, the TiO<sub>2</sub> layer could be compliantly covered by the PCBM interlayer, similar intimate contact to the top perovskite layer. PCBM was reported to prefer to form the hydrogen bond with defects OH<sup>-</sup> on TiO<sub>2</sub> surface and defects MA<sup>+</sup> on the perovskite surface to reduce interface defects and thereby passivate the non-radiative charge carrier recombination [39,40]. Moreover, as seen in Figure 8b, due to the hydrophobicity of the PCBM layer [25], compared to the perovskite grains growing on the TiO<sub>2</sub> layer shown in Figure 5a, the grain structure tended to be more compact with comparable uniform grain size and negligible pinholes. The dominant grain sizes were in the range of [300 nm, 450 nm] with an average value of 360 nm, a little bit larger in comparable to Figure 5. Large perovskite grain size was also supposed to reduce charge carrier combination via decreasing the amount of grain boundaries. Since the grain boundaries act as a kind of barrier to charge carriers' transportation, it increases the probability of non-radiative recombination. The reduction of pinholes between the perovskite grains facilitates the charge carriers' transportation by depressing the defect trap states located around the grain boundaries.

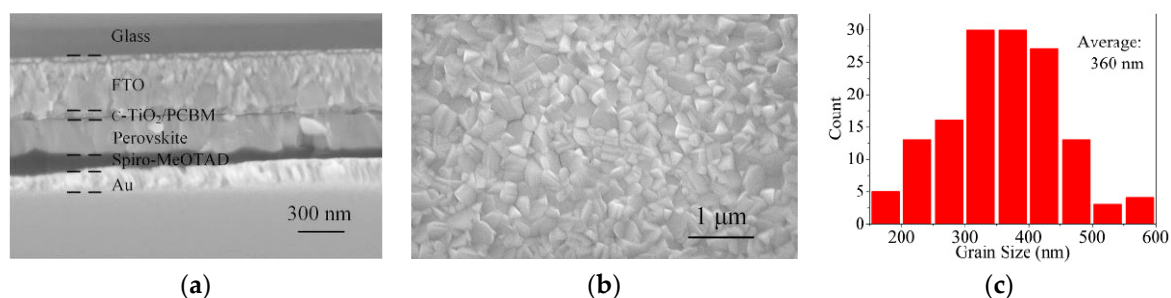


**Figure 8.** (a) Cross section, (b) surface SEMs of perovskite film with the PCBM interlayer and (c) the corresponding histogram of perovskite grain size distribution.

Steady-state photoluminescence (PL) measurements were performed to investigate the charge extraction efficiency of perovskite devices, as shown in Figure 9. Without introducing the PCBM interlayer, the enhanced PL intensity indicates the relatively poor electron extraction efficiency compared to that of the perovskite film passivated by the PCBM layer. The PCBM interlayer was proposed to passivate the interfacial defect traps between the perovskite and the TiO<sub>2</sub> layers, facilitating the photo-generated electrons extraction from the perovskite layer to the TiO<sub>2</sub>/PCBM domain, while restraining these electrons to flow back. In this case, even though there were massive photo-generated holes left in the perovskite layer (due to the lack of hole transport layer in the PL measurement), since the electrons were restricted in the TiO<sub>2</sub>/PCBM layer, the recombination should be limited,



leading to the quenched PL intensity [41]. A hysteresis test was performed on the PSCs with the PCBM interlayer, as illustrated in Figure 10. Although PCBM has excellent electrical conductivity compared to  $\text{TiO}_2$ , the transparency of the PSC might be affected due to the light transmittance of PCBM layer, influencing the light absorbing and current generation. We coated the PCBM film at 2000 rpm, 4000 rpm and 6000 rpm independently to testify the effect of the thickness of PCBM film on  $J-V$  parameters. All the devices present minor hysteresis in comparison to the results in Figure 7, implying decreased charge traps at the perovskite interface (perovskite/PCBM). These observations were in line with the fullerene-based solution-processed PSCs, suggesting PCBM could adapt to passivate  $J-V$  hysteresis in CVD-processed PSCs.  $J_{sc}$  was presented larger than that in Figure 7 without sharp reduction at forward scan, indicating PCBM passivation to decrease the charge carrier recombination. As to the device with PCBM layer coated at 2000 rpm,  $J_{sc}$  was about  $16 \text{ mA/cm}^2$ , minimum compared to that of 4000 rpm and 6000 rpm, suggesting too thick of a PCBM layer prohibited light transmission to the perovskite layer, reducing current generation. The best PCE performance of 12.2% for the reverse scan and 11.5% for the forward scan were obtained when the PCBM layer spun at 4000 rpm. The minimum FF difference reduced to about 6%, indicating excellent hysteresis passivation effect of PCBM layer by reducing interfacial recombination. Moreover, the dominant features for bulk recombination discussed previously, current bump and steep current drop at the beginning of the forward scan, were negligible after the PCBM interlayer was involved. It is proposed that the PCBM could penetrate into the perovskite grain boundaries during the CVD process via thermal annealing effect, as demonstrated in previous work [40], constructing continuous pathways for charge extraction through the bulk perovskite film. However, the other interfacial recombination occurred at the perovskite/Spiro-MeOTAD interface still worked as a barrier for charge extraction and thereby facilitated the existence of the slight hysteresis.

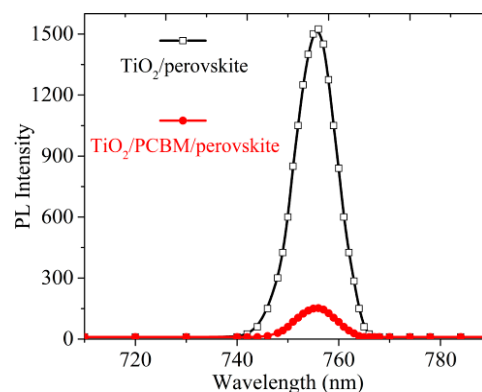


**Figure 9.** Steady-state photoluminescence (PL) curves of  $\text{TiO}_2$ /perovskite and  $\text{TiO}_2$ /PCBM/perovskite films.

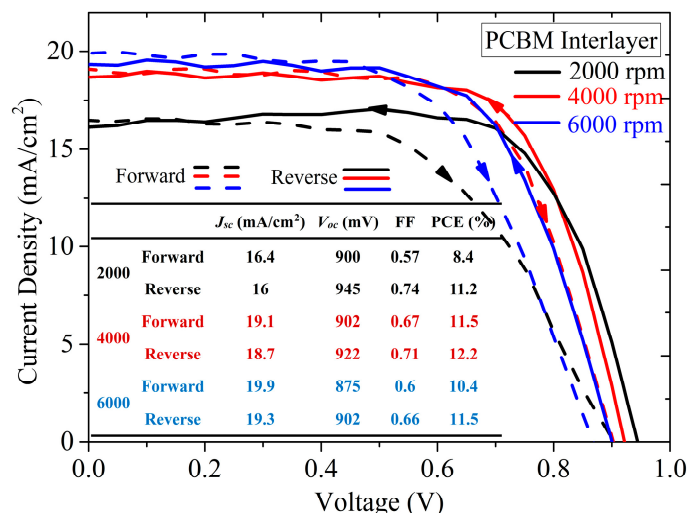


**Figure 10.**  $J$ - $V$  curves and corresponding photovoltaic performance of the PSC with PCBM interlayer with a scan step size of 20 mV and a standing time of 50 ms.

#### 4. Conclusions

In summary, we utilized a facile chemical vapor deposition (CVD) pattern, lead iodide (PbI<sub>2</sub>) substrates sandwich-surrounded by the source methyl-ammonium iodide (CH<sub>3</sub>NH<sub>3</sub>I, MAI) powder to fabricate methyl-ammonium lead iodide (MAPbI<sub>3</sub>) perovskite films. Numerical calculations using FLUENT software and the following experimental test illustrated that the proposed CVD pattern preferred to obtain a uniform distribution of MAI vapor and a homogeneous perovskite film with comparable surface morphologies, crystal structures and photovoltaic performances. As for the current density–voltage ( $J$ - $V$ ) curve hysteresis passivation, a PCBM ([6,6]-Phenyl C<sub>61</sub> butyric acid methyl ester) interlayer was introduced onto the titanium oxide (TiO<sub>2</sub>) layer before the PbI<sub>2</sub> coating and the CVD process. Results indicated that even suffering from the torturous CVD procedure, the PCBM still worked to passivating the hysteresis via reducing the bulk recombination and the interfacial recombination, similar as that in general solution-processed perovskite solar cells (PSCs). A uniform thickness of perovskite film and a compact perovskite grain structure were observed attributing to the passivation effect of the PCBM interlayer. Moreover, coupled with the excellent electron conductivity of the PCBM layer, the best power conversion efficiency (PCE) performance increased by 30%, and the filling factor (FF) difference between forward and reverse scan reduced to 6%. As for the further improvement of the PCE performance, it is a critical topic, which we are still working on. This work paved the way toward producing uniform perovskite layers using CVD procedure, and revealed the hysteresis passivation of the PCBM interlayer in the CVD-processed PSCs.

**Author Contributions:** Conceptualization, C.Y., X.S. and T.X.; methodology, C.Y.; software, C.Y.; validation, C.Y., X.S. and T.X.; formal analysis, C.Y.; investigation, C.Y.; resources, X.S.; data curation, C.Y.; writing—original draft preparation, C.Y.; writing—review and editing, C.Y. and X.S.; visualization, C.Y.; supervision, X.S. and T.X.; project administration, X.S. and T.X.; funding acquisition, X.S. and T.X.

**Funding:** This research was supported by the National Natural Science Foundation of China, grant number 51677043.

**Acknowledgments:** The authors gratefully acknowledgment the support from the State Key Laboratory of Precision Measurement Technology and Instruments in Tsinghua University, where the fabrication and characterization work were partially carried out.

**Conflicts of Interest:** The authors declare no conflict of interest.

## References

1. Liu, X.; Cheng, Y.; Liu, C.; Zhang, T.; Zhang, N.; Zhang, S.; Chen, J.; Xu, Q.; Ouyang, J.; Gong, H. 20.7% highly reproducible inverted planar perovskite solar cells with enhanced fill factor and eliminated hysteresis. *Energy Environ. Sci.* **2019**, *12*, 1622–1633. [[CrossRef](#)]
2. Yoo, J.J.; Wieghold, S.; Sponseller, M.C.; Chua, M.R.; Bertram, S.N.; Hartono, N.T.P.; Tresback, J.S.; Hansen, E.C.; Correa-Baena, J.-P.; Bulović, V.; et al. An interface stabilized perovskite solar cell with high stabilized efficiency and low voltage loss. *Energy Environ. Sci.* **2019**, *12*, 2192–2199. [[CrossRef](#)]
3. Turren-Cruz, S.H.; Hagfeldt, A.; Saliba, M. Methylammonium-free, high-performance, and stable perovskite solar cells on a planar architecture. *Science* **2018**, *362*, 449–453. [[CrossRef](#)] [[PubMed](#)]
4. Docampo, P.; Bein, T. A long-term view on perovskite optoelectronics. *Acc. Chem. Res.* **2016**, *49*, 339–346. [[CrossRef](#)]
5. Yang, D.; Zhou, X.; Yang, R.; Yang, Z.; Yu, W.; Wang, X.; Li, C.; Liu, S.; Chang, R.P.H. Surface optimization to eliminate hysteresis for record efficiency planar perovskite solar cells. *Energy Environ. Sci.* **2016**, *9*, 3071–3078. [[CrossRef](#)]
6. Chen, Q.; Zhou, H.; Hong, Z.; Luo, S.; Duan, H.S.; Wang, H.H.; Liu, Y.; Li, G.; Yang, Y. Planar heterojunction perovskite solar cells via vapor-assisted solution process. *J. Am. Chem. Soc.* **2013**, *136*, 622–625. [[CrossRef](#)]
7. Chen, Q.; Zhou, H.; Song, T.B.; Luo, S.; Hong, Z.; Duan, H.S.; Dou, L.; Liu, Y.; Yang, Y. Controllable self-induced passivation of hybrid lead iodide perovskites toward high performance solar cells. *Nano Lett.* **2014**, *14*, 4158–4163. [[CrossRef](#)]
8. Peng, Y.; Jing, G.; Cui, T. A hybrid physical–chemical deposition process at ultra-low temperatures for high-performance perovskite solar cells. *J. Mater. Chem. A* **2015**, *3*, 12436–12442. [[CrossRef](#)]
9. Peng, Y.; Jing, G.; Cui, T. High-performance perovskite solar cells fabricated by vapor deposition with optimized  $\text{PbI}_2$  precursor films. *RSC Adv.* **2015**, *5*, 95847–95853. [[CrossRef](#)]
10. Hsiao, S.Y.; Lin, H.L.; Lee, W.H.; Tsai, W.L.; Chiang, K.M.; Liao, W.Y.; Ren-Wu, C.Z.; Chen, C.Y.; Lin, H.-W. Efficient all-vacuum deposited perovskite solar cells by controlling reagent partial pressure in high vacuum. *Adv. Mater.* **2016**, *28*, 7013–7019. [[CrossRef](#)]
11. Shen, P.S.; Chen, J.S.; Chiang, Y.H.; Li, M.H.; Guo, T.F.; Chen, P. Low-pressure hybrid chemical vapor growth for efficient perovskite solar cells and large-area module. *Adv. Mater. Interfaces* **2016**, *3*, 1500849. [[CrossRef](#)]
12. Chen, J.; Xu, J.; Xiao, L.; Zhang, B.; Dai, S.; Yao, J. Mixed-organic-cation  $(\text{FA})_x(\text{MA})_{1-x}\text{PbI}_3$  planar perovskite solar cells with 16.48% efficiency via a low-pressure vapor-assisted solution process. *ACS Appl. Mater. Interfaces* **2017**, *9*, 2449–2458. [[CrossRef](#)] [[PubMed](#)]
13. Chen, Y.; Chen, T.; Dai, L. Layer-by-layer growth of  $\text{CH}_3\text{NH}_3\text{PbI}_{3-x}\text{Cl}_x$  for highly efficient planar heterojunction perovskite solar cells. *Adv. Mater.* **2015**, *27*, 1053–1059. [[CrossRef](#)] [[PubMed](#)]
14. Yin, J.; Qu, H.; Cao, J.; Tai, H.; Li, J.; Zheng, N. Vapor-assisted crystallization control toward high performance perovskite photovoltaics with over 18% efficiency in the ambient atmosphere. *J. Mater. Chem. A* **2016**, *4*, 13203–13210. [[CrossRef](#)]
15. Guo, Q.; Li, C.; Qiao, W.; Ma, S.; Wang, F.; Zhang, B.; Hu, L.; Dai, S.; Tan, Z.A. The growth of  $\text{CH}_3\text{NH}_3\text{PbI}_3$  thin film by simplified close space sublimation for efficient and large dimensional perovskite solar cells. *Energy Environ. Sci.* **2016**, *9*, 1486–1494. [[CrossRef](#)]
16. Lin, D.; Zhang, T.; Wang, J.; Long, M.; Xie, F.; Chen, J.; Wu, B.; Shi, T.; Yan, K.; Xie, W.; et al. Stable and scalable 3D-2D planar heterojunction perovskite solar cells via vapor deposition. *Nano Energy* **2019**, *59*, 619–625. [[CrossRef](#)]
17. Qiu, L.; He, S.; Jiang, Y.; Son, D.-Y.; Ono, L.K.; Liu, Z.; Kim, T.; Bouloumis, T.; Kazaoui, S.; Qi, Y. Hybrid chemical vapor deposition enables scalable and stable Cs-FA mixed cation perovskite solar modules with a designated area of  $91.8 \text{ cm}^2$  approaching 10% efficiency. *J. Mater. Chem. A* **2019**, *7*, 6920–6929. [[CrossRef](#)]
18. Zandi, S.; Razaghi, M. Finite element simulation of perovskite solar cell: A study on efficiency improvement based on structural and material modification. *Sol. Energy* **2019**, *179*, 298–306. [[CrossRef](#)]
19. Yang, C.; Simon, T.; Cui, T. Numerical simulation and analysis of hybrid physical-chemical vapor deposition to grow uniform perovskite  $\text{MAPbI}_3$ . *J. Appl. Phys.* **2017**, *121*, 144903. [[CrossRef](#)]
20. Cao, X.B.; Li, C.L.; Zhi, L.L.; Li, Y.H.; Cui, X.; Yao, Y.W.; Ci, L.J.; Wei, J.Q. Fabrication of high quality perovskite films by modulating the Pb-O bonds in Lewis acid-base adducts. *J. Mater. Chem. A* **2017**, *5*, 8416–8422. [[CrossRef](#)]

21. Im, J.H.; Jang, I.H.; Pellet, N.; Grätzel, M.; Park, N.G. Growth of  $\text{CH}_3\text{NH}_3\text{PbI}_3$  cuboids with controlled size for high-efficiency perovskite solar cells. *Nat. Nanotechnol.* **2014**, *9*, 927–932. [[CrossRef](#)] [[PubMed](#)]
22. Li, W.; Fan, J.; Li, J.; Mai, Y.; Wang, L. Controllable grain morphology of perovskite absorber film by molecular self-assembly toward efficient solar cell exceeding 17%. *J. Am. Chem. Soc.* **2015**, *137*, 10399–10405. [[CrossRef](#)]
23. Qiu, J.; McDowell, L.L.; Shi, Z. Room-temperature cubic perovskite thin films by three-step all-vapor conversion from PbSe to  $\text{MAPbI}_3$ . *Cryst. Growth Des.* **2019**, *19*, 2001–2009. [[CrossRef](#)]
24. Bi, C.; Wang, Q.; Shao, Y.; Yuan, Y.; Xiao, Z.; Huang, J. Non-wetting surface-driven high-aspect-ratio crystalline grain growth for efficient hybrid perovskite solar cells. *Nat. Commun.* **2015**, *6*, 7747. [[CrossRef](#)] [[PubMed](#)]
25. Wang, Q.; Chen, B.; Liu, Y.; Deng, Y.; Bai, Y.; Dong, Q.; Huang, J. Scaling behavior of moisture-induced grain degradation in polycrystalline hybrid perovskite thin films. *Energy Environ. Sci.* **2017**, *10*, 516–522. [[CrossRef](#)]
26. Liang, P.W.; Chueh, C.C.; Williams, S.T.; Jen, A.K.Y. Roles of fullerene-based interlayers in enhancing the performance of organometal perovskite thin-film solar cells. *Adv. Energy Mater.* **2015**, *5*, 1402321. [[CrossRef](#)]
27. Fu, F.; Feurer, T.; Jager, T.; Avancini, E.; Bissig, B.; Yoon, S.; Buecheler, S.; Tiwari, A.N. Low-temperature-processed efficient semi-transparent planar perovskite solar cells for bifacial and tandem applications. *Nat. Commun.* **2015**, *6*, 8932. [[CrossRef](#)]
28. Shao, Y.; Xiao, Z.; Bi, C.; Yuan, Y.; Huang, J. Origin and elimination of photocurrent hysteresis by fullerene passivation in  $\text{CH}_3\text{NH}_3\text{PbI}_3$  planar heterojunction solar cells. *Nat. Commun.* **2014**, *5*, 5784. [[CrossRef](#)]
29. Yang, C.; Peng, Y.; Simon, T.; Cui, T. Control of  $\text{PbI}_2$  nucleation and crystallization: Towards efficient perovskite solar cells based on vapor-assisted solution process. *Mater. Res. Express* **2018**, *5*, 045507. [[CrossRef](#)]
30. Platten, J.K. The soret effect: A review of recent experimental results. *J. Appl. Mech. Trans. ASME* **2006**, *73*, 5–15. [[CrossRef](#)]
31. Wang, B.; Young Wong, K.; Xiao, X.; Chen, T. Elucidating the reaction pathways in the synthesis of organolead trihalide perovskite for high-performance solar cells. *Sci. Rep.* **2015**, *5*, 10557. [[CrossRef](#)] [[PubMed](#)]
32. Li, X.; Bi, D.; Yi, C.; Décoppet, J.D.; Luo, J.; Zakeeruddin, S.M.; Hagfeldt, A.; Grätzel, M. A vacuum flash-assisted solution process for high-efficiency large-area perovskite solar cells. *Science* **2016**, *353*, 58–62. [[CrossRef](#)] [[PubMed](#)]
33. Nemnes, G.A.; Besleaga, C.; Tomulescu, A.G.; Palici, A.; Pintilie, L.; Manolescu, A.; Pintilie, I. How measurement protocols influence the dynamic JV characteristics of perovskite solar cells: Theory and experiment. *Sol. Energy* **2018**, *173*, 976–983. [[CrossRef](#)]
34. Liu, Y.; Akin, S.; Pan, L.; Uchida, R.; Arora, N.; Milić, J.V.; Hinderhofer, A.; Schreiber, F.; Uhl, A.R.; Zakeeruddin, S.M.; et al. Ultrahydrophobic 3D/2D fluoroarene bilayer-based water-resistant perovskite solar cells with efficiencies exceeding 22%. *Sci. Adv.* **2019**, *5*, eaaw2543. [[CrossRef](#)]
35. Courtier, N.E.; Cave, J.M.; Foster, J.M.; Walker, A.B.; Richardson, G. How transport layer properties affect perovskite solar cell performance: Insights from a coupled charge transport/ion migration model. *Energy Environ. Sci.* **2019**, *12*, 396–409. [[CrossRef](#)]
36. Wang, F.; Shimazaki, A.; Yang, F.; Kanahashi, K.; Matsuki, K.; Miyauchi, Y.; Takenobu, T.; Wakamiya, A.; Murata, Y.; Matsuda, K. Highly efficient and stable perovskite solar cells by interfacial engineering using solution-processed polymer layer. *J. Phys. Chem. C* **2017**, *121*, 1562–1568. [[CrossRef](#)]
37. Peng, J.; Wu, Y.; Ye, W.; Jacobs, D.A.; Shen, H.; Fu, X.; Wan, Y.; Duong, T.; Wu, N.; Barugkin, C.; et al. Interface passivation using ultrathin polymer-fullerene films for high-efficiency perovskite solar cells with negligible hysteresis. *Energy Environ. Sci.* **2017**, *10*, 1792–1800. [[CrossRef](#)]
38. Yoon, H.; Kang, S.M.; Lee, J.K.; Choi, M. Hysteresis-free low-temperature-processed planar perovskite solar cells with 19.1% efficiency. *Energy Environ. Sci.* **2016**, *9*, 2262–2266. [[CrossRef](#)]
39. Cai, F.; Yang, L.; Yan, Y.; Zhang, J.; Qin, F.; Liu, D.; Cheng, Y.-B.; Zhou, Y.; Wang, T. Eliminated hysteresis and stabilized power output over 20% in planar heterojunction perovskite solar cells by compositional and surface modifications to the low-temperature-processed  $\text{TiO}_2$  layer. *J. Mater. Chem. A* **2017**, *5*, 9402–9411. [[CrossRef](#)]

40. Xu, J.; Buin, A.; Ip, A.H.; Li, W.; Voznyy, O.; Comin, R.; Yuan, M.; Jeon, S.; Ning, Z.; McDowell, J.J. Perovskite-fullerene hybrid materials suppress hysteresis in planar diodes. *Nat. Commun.* **2015**, *6*, 7081. [[CrossRef](#)]
41. Tao, C.; Neutzner, S.; Colella, L.; Marras, S.; Srimath Kandada, A.R.; Gandini, M.; Bastiani, M.D.; Pace, G.; Manna, L.; Caironi, M.; et al. 17.6% stabilized efficiency in low-temperature processed planar perovskite solar cells. *Energy Environ. Sci.* **2015**, *8*, 2365–2370. [[CrossRef](#)]



© 2019 by the authors. Licensee MDPI, Basel, Switzerland. This article is an open access article distributed under the terms and conditions of the Creative Commons Attribution (CC BY) license (<http://creativecommons.org/licenses/by/4.0/>).